Universität Hamburg
Fachbereich Informatik
Vogt-Kölln-Str. 30
D-22527 Hamburg

Bericht 255

Laser Scanning Microscopy Flatfield Images

Part I: Characterization of Noise Properties

FBI-HH-B-255/03

Christian-Dennis Rahn
Universität Hamburg
Fachbereich Informatik
rahn@informatik.uni-hamburg.de

In die Reihe der Berichte des Fachbereichs Informatik aufgenommen durch
Prof. Dr. H. S. Stiehl
Prof. Dr. B. Neumann

Dezember 2003

Laser Scanning Microscopy Flatfield Images Part I: Characterization of Noise Properties

Christian-Dennis Rahn*

University of Hamburg
Dept. of Informatics
Cognitive Systems Laboratory (KOGS)
Vogt-Kölln-Str. 30
22527 Hamburg
Germany

Beiersdorf AG
Analytical Microscopy Dept.
Troplowitzstr. 15
20245 Hamburg
Germany

10th December 2003

*e-Mail: rahn@informatik.uni-hamburg.de

Abstract

Noise may be a great obstacle to automatic processing and analysis of measured data. In order to reduce noise several methods exist. However, all of the individual methods have their strengths and weaknesses, which may heavily depend on the origin of data to be processed. Therefore, in certain circumstances it may be a necessity to characterize the properties of the noise present in the data of interest, and then select the most suitable method for either pre-processing or direct analysis based on that information. This is especially true in the context of automatic image analysis.

This first part of a report pair examines in a detailed manner the noise properties of two dedicated 2D flatfield digital image series acquired with a multi photon laser scanning microscope (MPLSM). The main result is that noise in the given images varies notably with local pixel intensity, and that this fact should be kept in mind when processing image data acquired by this instrument.

Zusammenfassung

Rauschen kann eine automatische Verarbeitung oder Analyse von gemessenen Daten erheblich behindern. Es existieren zwar zahlreiche Methoden zur Reduktion von Rauschen, jedoch besitzt jede einzelne Methode ihre speziellen Stärken und Schwächen, welche stark vom jeweiligen Ursprung der zu verarbeitenden Daten abhängen können. Deshalb kann es im Einzelfall notwendig sein, die Eigenschaften des Rauschens in den Daten zu charakterisieren, um dann eine geeignete Methode der Vorverarbeitung oder der direkten Analyse auszuwählen. Dies gilt besonders im Falle automatischer Datenanalyse.

In diesem ersten Teil eines Bericht-Paares werden in detailierter Weise die Rausch-Eigenschaften zweier sog. *Flatfield*-Bildserien untersucht. Diese Bildserien wurden mittels Multiphotonen-Laser-Rastermikroskopie (MPLSM) gewonnen. Das Hauptergebnis dieser Arbeit ist, dass in den untersuchten Bildern das Rauschen deutlich mit der lokalen Pixel-Intensität variiert. Diese Tatsache sollte beachtet werden, wenn mit dem verwendeten Mikroskop aufgenommene Bilddaten verarbeitet werden sollen.

1 Introduction

Depending on the actual context *de-noising* can be an important step in low-level image processing. In fact, it can be a crucial step prior to the successful automatic analysis of measured data. Since plenty of methods are available for de-noising images and several techniques for robust analysis, all of which differ in their performance, as e.g. quality of the result, speed of operation, availability in present software tools, degree of user adjustment, one has to wisely choose and adjust a single method to achieve the given task. Here, quantitative properties of the actual noise present in the data are a prerequisite for choosing the appropriate method.

For this work, suitable phantom image data acquired by MPLSM are examined to characterize the noise properties of fluorescence imaging. Technical details of the imaging principle and the fluorescence effect can be found in [1] and [2] for example.

There are numerous sources of noise (see [4] for details) in laser scanning microscopy, as e.g. noise in electronic circuits, thermic noise, and detector noise due to low light intensities. This is especially true when using fluorescence imaging, which acts in a very low intensity regime. Additionally, the signal-noise-ratio (SNR) will be further decreased in the case of in-vivo imaging, where illumination intensities have to be balanced with potential photo toxicity damaging the imaged tissue. Contrast-enhancing treatment of the subject, as e.g. dye injection, may be too invasive to the structures of interest. Also, increasing the pixel dwell time may be no viable option here, since acquisition of a 3D image stack of reasonable size takes non neglectable time. More efficient detectors can be very costly or may not be available at all. So, a priori noise reduction at the imaging hardware level is not in every case possible.

Since very low light intensities constitute the imaging, the acquisition can be modeled as a Poisson process. This fact is well confirmed here and described in the following sections, but this examination itself is not founded on this imaging model. A more general approach to the problem has been taken.

The rather general methods to examine the given image data used in this work should be suitable also for other kinds of signals having at least a dimensionality of one.

This report is organized as follows: First, some notes on the acquisition of the examined images will be given. Then the generation of a reference image to be used as ground

truth for the examinations is described. A large section discussing the results about the image noise follows, and lastly some conclusions will be drawn.

2 Data Acquisition

In the present work, two distinct sets A and B of consecutively taken images of the same scenery, each set of $N = 10$ members, have been examined. For acquisition, a *DermaInspect 100* (JenLab, Jena, Germany) MPLSM has been used. This instrument illuminates the field of view by a scanning laser of the tuneable excitation wavelength λ_{ex}. Emitted fluorescence light coming mainly from the illumination beam focus point will be collected by a very sensitive photo multiplier tube (PMT), which counts electrons produced by incoming photons due to the *photoelectric effect*. The number of *photo electrons* is proportional to the fluorescence light intensity and will be mapped linearly to a gray-level ready for on-screen display.

The used microscope has the peculiarity of a rather strong intensity shading (details to follow), which is as mentioned above a prerequisite for our investigation. For all images of a series, every imaging parameter was kept unchanged and hence differences between single images only result from noise.

The first set of images $I_{A,i}$, $i \in T = \{1,\ldots,N\}$, was acquired at a two-photon fluorescence excitation wavelength of $\lambda_{ex,A} = 750\text{nm}$, while the second series[1] $I_{B,i}$ was acquired at $\lambda_{ex,B} = 850\text{nm}$. The wavelength λ_{em} of the emission spectrum maximum intensity is typically quite above the half of the excitation wavelength and depends on the actual type of specimen molecules. Both series differ in global intensity, since the efficiency of the fluorescence effect for a given substance as well as the detector efficiency is a function of the actual excitation or emission wavelength respectively. Despite the different λ_{ex}, all other instrument parameters stayed unchanged. However, for the used microscope the actual physical parameters may vary implicitly for different instrument adjustments, as for example the true photon flux of the illumination laser depends on the laser wavelength. This too effects the global image intensity. The actually used range of instrument parameters, as e.g. nominal laser intensity, magnification, lenses, signal amplification, pixel

[1] Since both image sets are treated in the same way, the subscripts A and B will be left out in the following.

dwell time, etc. were adjusted as in a typical specimen imaging situation. The image size in pixels is 512×512 and the intensity quantization is 8bit; the actual optical resolution and magnification, are of no interest here.[2]

The imaged scenery is a plain fluorescein solution (Aqueous solution, Sigma Chemical, St. Louis, USA), presented on a small microscope slide, covered by a microscope cover glass. The imaged plane was right in the middle of the liquid volume.

Imaging the described scenery should result in homogenous intense *flatfield images* C, ideally showing no structures, i.e. $C(\mathbf{x}) = const$. In fact, a rather strong *shading* caused by uneven illumination modulates spatially the measured intensity, which is strongest in about the field of view center, and vanishes to the field border. It can be shown that the shape of the modulation function is quite close to a 2D Gaussian bell function (see [7]). In fact, this shading is a benefit and even substantial for the work presented here. Two typical flatfield images of both image sets can be seen in fig. 1.

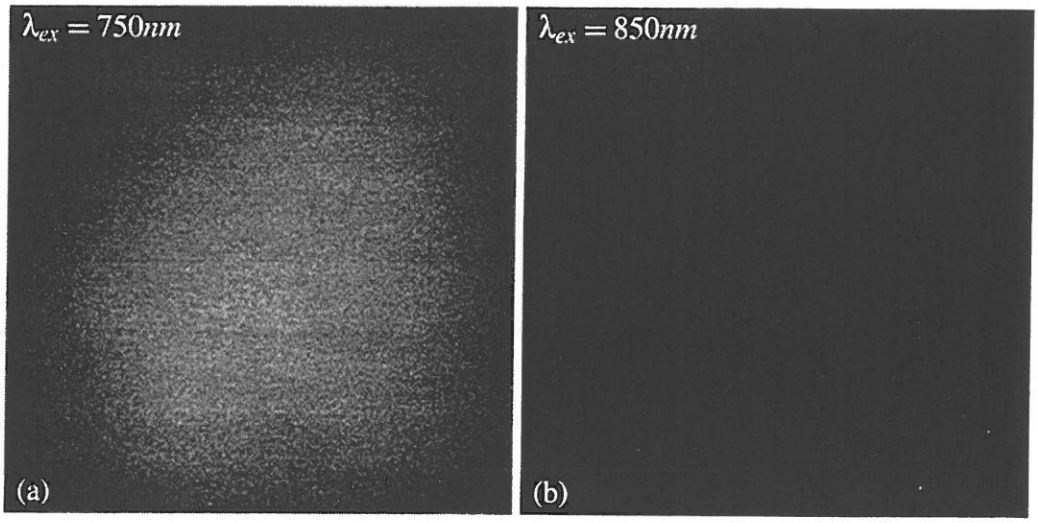

Figure 1: Shown are two MPLSM flatfield sample images. (a) Excitation wavelength: 750nm. (b) Excitation wavelength: 850nm. The strong intensity shading effect is clearly visible.

In order to compactly describe measured data $Z = (z_1, \ldots, z_n)^T$ consisting of n sam-

[2] In the case of e.g. confocal imaging, the actual aperture size, i.e. the pinhole size, relates to the size of the effectively excited volume and thus the aperture not only effects the actual spatial resolution but also the number of photons taking part in the imaging process. Hence, an eventual aperture size would be of interest here.

ples, we make in this work much use of the *mean* $\langle Z \rangle$ and the unbiased *standard deviation* $StD[Z]$ of the data set, which are defined in a standard way by:

$$\langle Z \rangle = \frac{1}{n} \sum_{i=1}^{n} z_i \,, \quad Std[Z] = \sqrt{\frac{1}{n-1} \sum_{i=1}^{n} (z_i - \langle Z \rangle)^2} \tag{1}$$

3 Reference Image

In order to characterize the noise in given data, it would be necessary to know the true function values without noise, i.e. the so-called *ground truth*. Typically, this information is not available for measured data. So, let a *reference image* $\bar{I}$ be an estimation of the shaded ground truth image C. For this estimation, the static scenery has been repeatedly imaged to produce a set $\{I_i\}$ of images. Each individual image I_i in the set is then compared to this reference image.

A reference image $\bar{I}$ can be generated in several ways:

Averaging of the whole image set $\{I_i\}$ pixel by pixel, or, synonymously: *time-filtering*. This enhances the quality of the reference image in terms of the SNR approx. by a factor of $\sqrt{N}$, with N being the number of images to be averaged.

Model fitting to each individual image I_i. If a parametric model function exists that sufficiently fits the data, this route can be taken. The main advantage is that fluctuations between the individual images (such as *lateral drift*) can be damped effectively. But model fitting may require high computational effort.

Spatial low-pass filtering of each individual image. This is a quite simple method, but it may degrade severely the quality of the expected results, since the low-pass filtering *blurs* the obtained intensity value distributions (described later).

In this work, averaging will be used to generate a reference image: $\bar{I}(\mathbf{x}) = \langle \{I_i(\mathbf{x})\} \rangle$. Model fitting is also a nice option, but it heavily depends on finding the right parametric function and of course the function fitting very well the data. For the actual data, a very good model can be found, but the data showed sporadic deviations from the model (i.e. "notches", see [7]). As a consequence image averaging seems to be preferable.

3.1 Verification of Comparability

Before comparing the noise properties of several images I_i to a certain reference image $\bar{I}$, it is necessary to verify that all images are in perfect *alignment*. Since the geometry of the used optics is very sensible to perturbations (floor vibrations, etc.) during an image acquisition session, a lateral drift of the scenery or a drift of the shading may occur even for a relative short image series. Such a drift would blur any image comparison results, and mutual translations of the images I_i would also degrade the quality of the reference image $\bar{I}$.

For alignment verification purposes pure global field measures are needed for the given images, since they do not contain any local structures possibly acting as *landmarks* for the alignment. At this place we are not interested in describing the image scenery in a detailed manner. In our case a simplified but robust description of the scenery suffices. The so-called *image moments* stemming directly from multivariate descriptive statistics (see [8] for further explanation) are measures that fullfill these requirements.[3] The moments compactly describe the location, orientation, and extension of structures in images. Here the moments can be calculated for each of the given images as a whole.

Let Ω be the discrete imaged n-dimensional field of view, then the zeroth and first order moments for a monochrome digital image $I(\mathbf{x})$, with $\mathbf{x} = (x_i) = (x_1, \ldots, x_n)^T$, can be calculated as follows (simplified eqs.):

$$M = \sum_{\mathbf{x}\in\Omega} I(\mathbf{x}) \tag{2}$$

$$\mathbf{m} = \frac{1}{M} \sum_{\mathbf{x}\in\Omega} I(\mathbf{x}) \cdot \mathbf{x} \tag{3}$$

Furthermore, we use the central moments of second order, which can be compactly written as the symmetric and positive definite *covariance matrix* $\mathbf{K}$:

$$\mathbf{K} = \frac{1}{M} \sum_{\mathbf{x}\in\Omega} I(\mathbf{x}) \cdot (\mathbf{x}-\mathbf{m}) \cdot (\mathbf{x}-\mathbf{m})^T \tag{4}$$

As a shortcut for the diagonal elements of $\mathbf{K} = (K_{i,j})$, we define $V_i = \sqrt{K_{i,i}}$. For the present 2D case of images $i, j \in \{1,2\}$ enumerate the dimensions of the data, and only

[3] In literature one can find, that the central moments are not very robust measures to describe arbitrary random distributions (e.g. see [5]). This fact is not a problem in our case, since plenty of samples forming the image of a 2D Gaussian bell function are accumulated for each moment estimation.

one single off-diagonal element of the 2×2-matrix $\mathbf{K}$ remains, which we combine here into the *correlation coefficient*:

$$CO = \frac{(K_{1,2})^2}{K_{1,1} \cdot K_{2,2}} \,. \tag{5}$$

However, the previous equations (2) to (4) are also applicable for higher dimensional data, as e.g. volume data. In mechanical terms the preceding equations describing *mass inertia moments* can be interpreted as follows: The intensity $I(\mathbf{x})$ can be seen as local density, M is the mass of the whole scenery, the point $\mathbf{m} = (m_i)$ is the center of gravity, and the eigenvectors of $\mathbf{K}$ are the main axes of inertia of the scenery while the according eigenvalues measure the extension along the main axes respectively. However, for our mere verification purpose we do not need to compute the eigensystem at this place. Instead it is sufficient to use V_1, V_2, and CO. The V_i measure the anisotropic structure extension along the image axes, and $CO \in [0, 1]$ varies with the orientation of the shading shape within the image. For $CO = 0$ the structure is oriented perfectly parallel to one of the image axes, and it is most diagonal oriented for the case of $CO = 1$. The basic assumption behind the central moments is a Gaussian bell-like, i.e. strongly clustered, density distribution of the data.

3.1.1 Results of Alignment Verification

Computational results of the above moments for the two image series are given in the tables 1 and 2. They show, that the central point $\mathbf{m}$ (which equals the global maximum here) of the shading shape does not drift a whole pixel between images (the respective deviations are all well below 1), which indeed is a very good result. Also, the variations of the V_1 and V_2 (i.e. the shape extension) values within each series are far below 1 percent. The CO-parameter has values of about 10^{-4}, which means that V_1 and V_2 are practically not correlated, and hence the shading shape is oriented as the image coordinate system. The orientation value CO can therefore be neglected here.

The preceeding results show that all images of a series are nearly the same in terms of the above image moments, and therefore a reliable reference image generation by averaging is assumed.[4]

[4]That the individual results (see the last rows in tables 1 and 2) for both image series differ noticeably although both series have been taken subsequently, gives another hint why this verification step is necessary.

#	m_1	m_2	V_1	V_2	$CO/10^{-4}$
1	259.422	268.479	189.005	187.882	2.45
2	259.248	269.416	188.760	188.188	1.86
3	258.831	270.269	188.642	187.378	1.48
4	258.946	270.128	188.734	187.562	1.74
5	258.675	270.407	188.710	187.492	1.63
6	258.861	270.292	188.747	187.635	1.52
7	258.862	270.880	188.798	187.839	1.95
8	258.985	270.538	188.891	188.049	2.48
9	258.998	270.287	188.870	187.482	1.81
10	258.999	270.155	188.873	187.372	1.77
	259.0 ± 0.2	270.1 ± 0.7	188.8 ± 0.1	187.7 ± 0.3	1.9 ± 0.3

Table 1: Central image moments for the 750nm series. The last row contains the respective mean values and standard deviations.

#	m_1	m_2	V_1	V_2	$CO/10^{-4}$
1	251.956	250.780	185.157	190.611	5.18
2	251.960	250.908	185.269	190.387	6.45
3	251.957	251.072	185.312	190.391	7.66
4	251.756	250.832	185.303	190.718	7.44
5	251.764	251.036	185.277	190.686	6.59
6	252.001	250.846	185.262	190.439	6.21
7	251.434	251.245	185.247	190.595	6.23
8	251.652	251.063	185.282	190.182	7.58
9	251.989	250.914	185.297	190.405	6.84
10	251.797	250.790	185.308	190.539	7.32
	251.8 ± 0.2	251.0 ± 0.2	185.3 ± 0.1	190.5 ± 0.2	6.8 ± 0.8

Table 2: Central image moments for the 850nm series. The last row contains the respective mean values and standard deviations.

4 Discussion

4.1 Spatial Intensity Variability

The term *spatial variability* of the noise characterizes the actual amount of noise present at a certain position $\mathbf{x}$ within the image field. This intensity uncertainty $SD(\mathbf{x})$ can be subjectively guessed from fig. 2. For each pixel position $\mathbf{x} \in \Omega$, the standard deviation of the intensity set of all images I_i at that position is shown as a gray-level coding ($SD(\mathbf{x}) = StD[\{I_i(\mathbf{x})\}]$). As can be seen in the two upper images, the "direct border pixels" may show a significantly higher intensity variability than "near border pixels", which is likely an effect of the scanning unit of that particular microscope.

For a better visual impression, all the border pixels in the whole image set (a five pixels wide frame) have been set to a value of zero denoted here as *border clearance*. Doing so enhances the contrast of the deviation images for a human observer (lower two images in fig. 2). It can be easily seen then and shown by simple image subtraction (data not presented), that the pixel-wise intensity variability resembles quite well the appearance of the flatfield images themselves. This allows two different interpretations:

(1) The variability is a function of the local scene intensity: $SD(\mathbf{x}) = f(C(\mathbf{x}))$, or

(2) the variability is merely a function of location: $SD(\mathbf{x}) = f(\mathbf{x})$.

Given the optical geometry of the used instrument, interpretation (1), namely that the noise is a function of intensity and not of position within the field of view, seems more likely. Images of structured specimen support this assumption. Only the border pixels are following interpretation (2), have a low prediction reliability, and therefore should be omitted for quantitative image analysis.

Strictly speaking, the modulation caused by the shading effect results implicitly in a spatial variability of intensity as well. In section 4.2.2 it will become clear that this is only a minor effect.

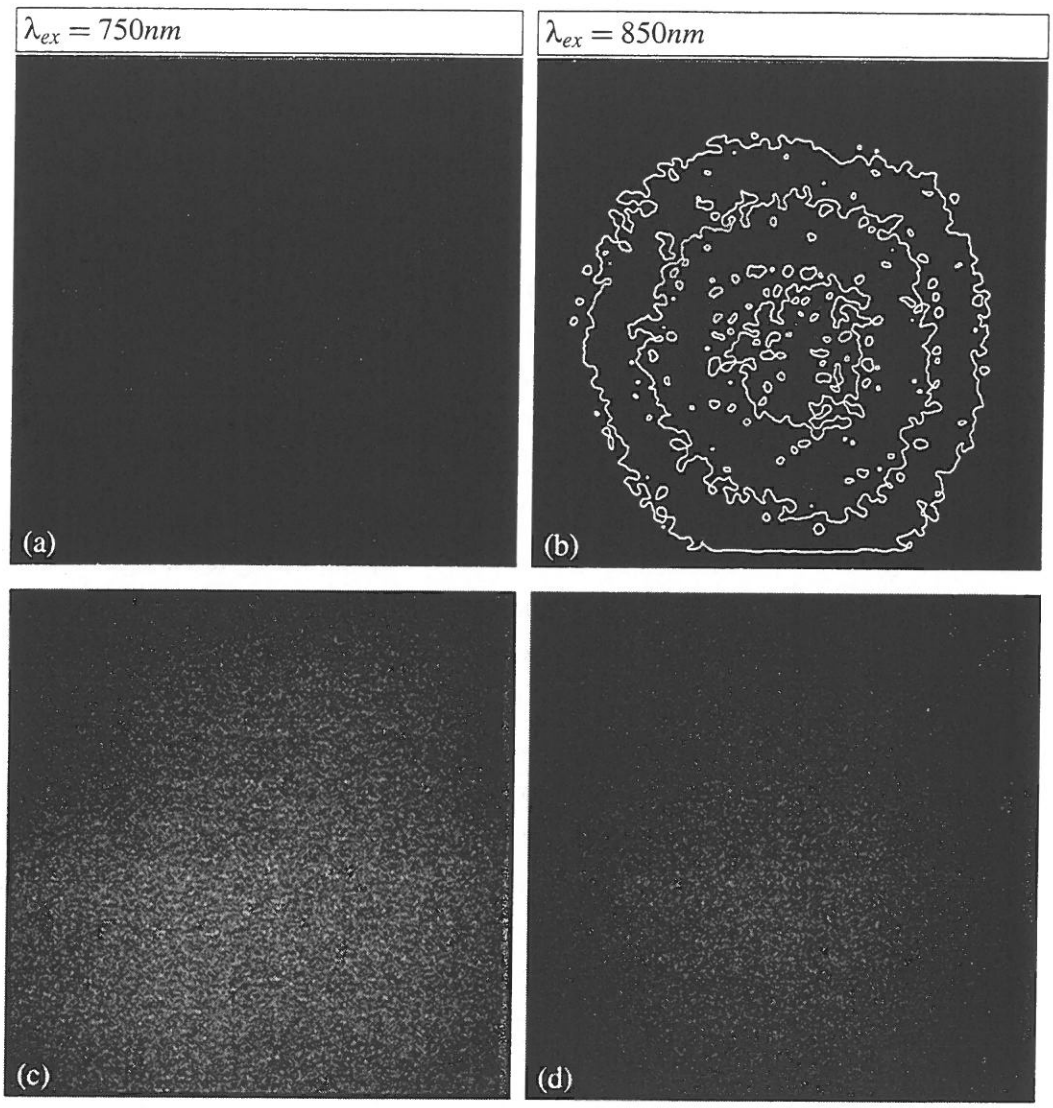

Figure 2: The standard deviation of the intensity dispersion on the whole image series per pixel is shown as a gray-level density plot. *Top row* The pixel standard deviations as directly measured. On density plot (b) a strongly smoothed contour plot showing three levels has been superimposed. *Bottom row* The standard deviations measured under omission of the border pixels, which tend to show a very high variability. This enhances the contrast in the center. Here, a maximum of variation can be seen at the field center.
All images are shown with spread contrast. The left column shows the values taken at 750nm, whereas the right column shows the values for 850nm wavelength.

4.2 Global Intensity Variability

4.2.1 Full Field Intensity Dispersion

In order to abstract from the position $\mathbf{x}$ within the field of view and to focus more on the actual local noise itself, the values of all pixels having the same reference intensity g throughout the full image series[5] I_i were collected in a dispersion set D_g:

$$D_g := \{I_i(\mathbf{x}) \mid \bar{I}(\mathbf{x}) = g,\ \mathbf{x} \in \Omega,\ i \in T\} \tag{6}$$

Mean $\langle D_g \rangle$ and standard deviation $StD[D_g]$ for each reference intensity g are shown in fig. 3. The mean shows of course a linear relation with a slope of exactly 1 here, while the standard deviation is linear only at a first approximation. The large error bars at the lower end (750nm: $x < 30$ and 850nm: $x < 10$) of both curves stem from the strong noisiness at the image border as already mentioned above. Again, setting the image border pixels to zero, normalizes the plots very well at the lower end (not shown). Since the actual number of samples (i.e. $|D_g|$), which span a rather large range of ca. 100 to 35000 (see the upper histogram plot in fig. 5), does not affect too much the nearly linear behavior, a good quality of the shown estimations is assumed.

The remarkably precise linear relation between g and $\langle D_g \rangle$ having a factor of 1, which one would of course expect, renders the used type of reference image $\bar{I}$ a good choice: the intensity variations account for the signal noise and not for the averaging of spatial structures.

With border clearance applied, fig. 4 plots for both image series the *coefficient of variation* ($CV[X] := StD[X]/\langle X \rangle$) of the intensity with respect to the according reference intensity. The non-constant factor between standard deviation and mean gives the impression, that $StD \propto g$ only holds in the sense of a first approximation. The reason for the quite different slopes at different excitation wavelengths will be clarified in section 4.2.3.

In fig. 5 the respective standard deviations for g from fig. 3 are shown directly vs. the reference intensity. Here, the particular nonlinearity is more visible. In fact, the upper curve for 750nm is well describable (at least in the main operating range) by a power

[5] Another option would be to just collect all those pixels within one single image, and then compare plots like fig. 3 for all images. This has not been done here.

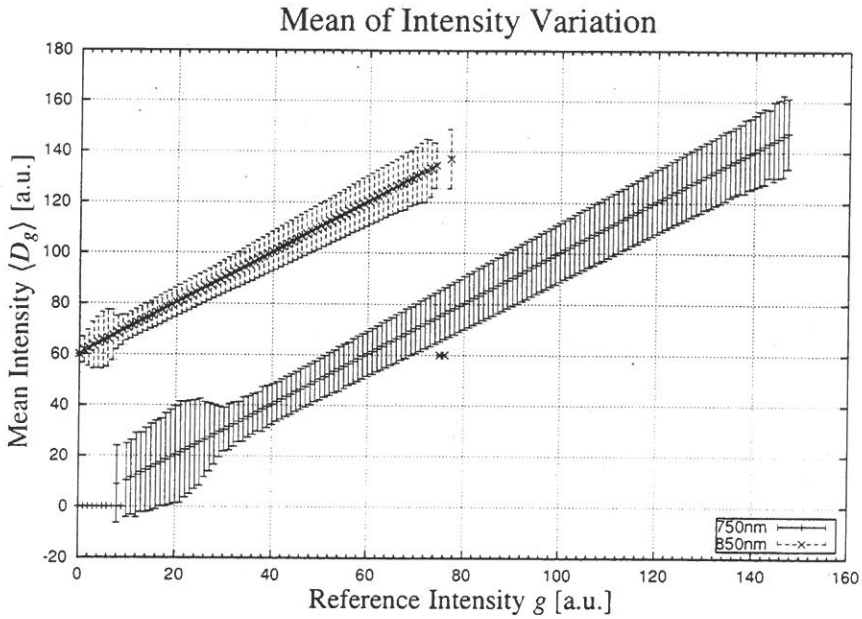

Figure 3: This plot shows the intensity averaged throughout the image series vs. the reference intensity. The error bars show the respective standard deviation. The upper curve for 850nm is transposed by a bias of 60, to enhance visual differentiability. Both curves start at the origin and have a slope of 1.

function

$$SD[g] = a + \sqrt{g - b} \tag{7}$$

with the parameters $a = 3.04$, and $b = 26.2$, as shown in the plot. For the 850nm curve such a fit results in $a = 3.74$, and $b = 23.12$. The rationale for this nonlinear relation will be given in the following section.

4.2.2 Single Intensity Dispersion

Every single reference intensity g manifests itself in an individual noise distribution. The distributions for all possible intensities g do not share the same shape. As can be seen from figs. 3 and 6, the distribution width is almost proportional to g. A detailed view on this assumed proportionality follows later.

Fig. 6 also contains exemplary nonlinear least squares fits of Gaussian normal distributions modeling the respective sampled distribution. The probability distribution function (PDF) for a Gaussian normal distributed random value z having mean μ and standard

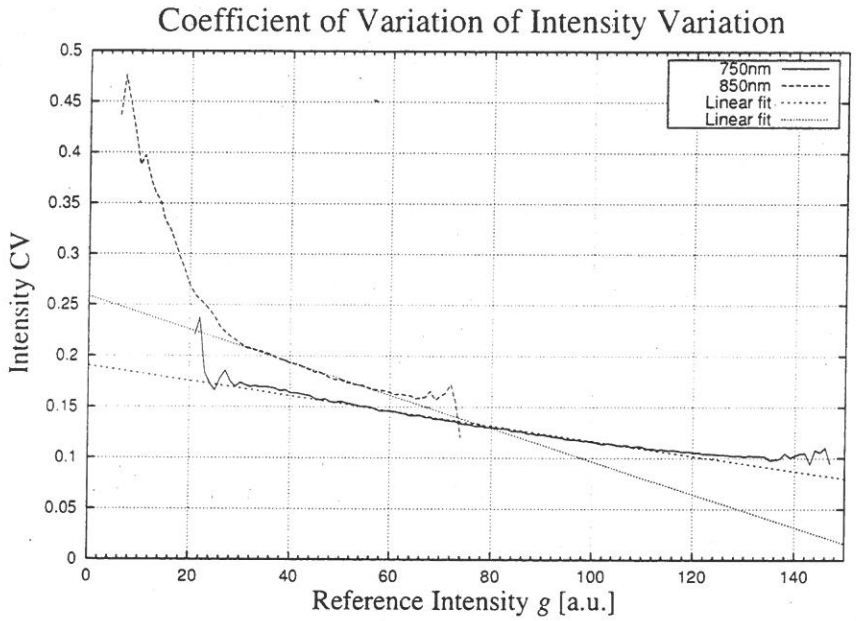

Figure 4: Coefficient of Variation of global intensity variation. The open left ends of both curves are due to the border clearance. The strong noisy deviations of linearity stem mainly from the respective low sample number.

deviation σ is given by:

$$p_G(z;\mu,\sigma) = \frac{1}{\sqrt{2\pi}\sigma} \exp\left[-\frac{1}{2}\left(\frac{z-\mu}{\sigma}\right)^2\right] \tag{8}$$

In our case, z is the actually measured intensity, while $\mu = g$ represents the respective reference intensity. According to the plot the fits are very accurate. The systematic asymmetry or *positive skew*[6] that is visible in the plots (left tail of data is below the Gaussian prediction and vice versa for the right tail) stems from the fact that imaging of the stochastic fluorescence photons (which are in fact generated by a quantum mechanical process) is actually a *Poisson process* having the following discrete probability function:

$$p_P(z;\mu) = \exp(-\mu)\frac{\mu^z}{z!} \tag{9}$$

Now, for increasing mean values μ, Poisson distributions approximate asymptotically a corresponding Gaussian normal distribution (details can be found in any text book on

[6]The *skewness* of a distribution is related to its 3rd central moment.

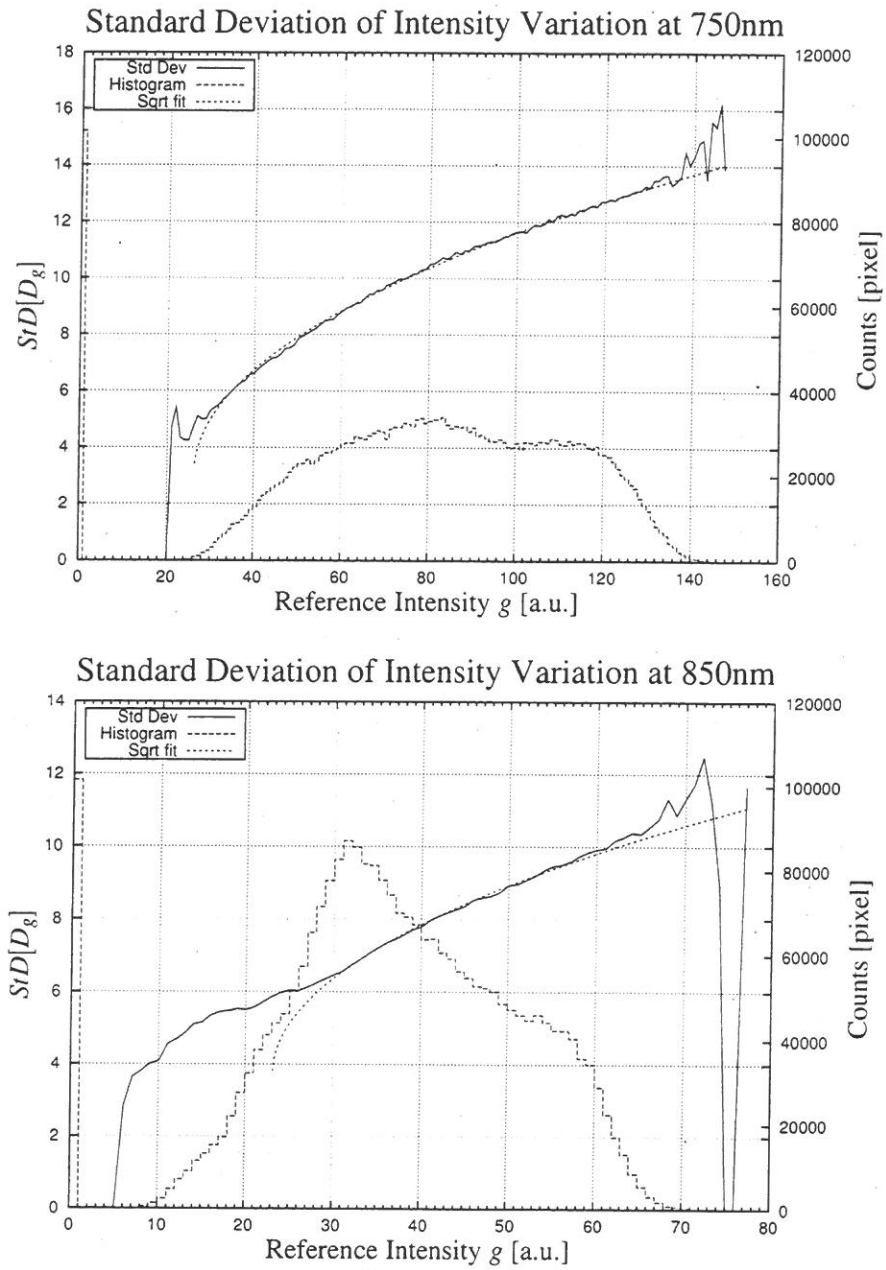

Figure 5: Global intensity variability. Shown is the standard deviation from fig. 3. The large number of zero intensity pixels in both plots is due to the mentioned border clearance. A standard deviation of 0 in the curves does not state absolute certainty, but merely that not enough pixels of the according reference intensity could be accounted for an estimation. The pixel counts have been included to give a hint on the certainty of each deviation estimation. The fits have been restricted to $30 \leq g \leq 110$ for the upper plot, and $30 \leq g \leq 60$ for the lower. See text for further description.

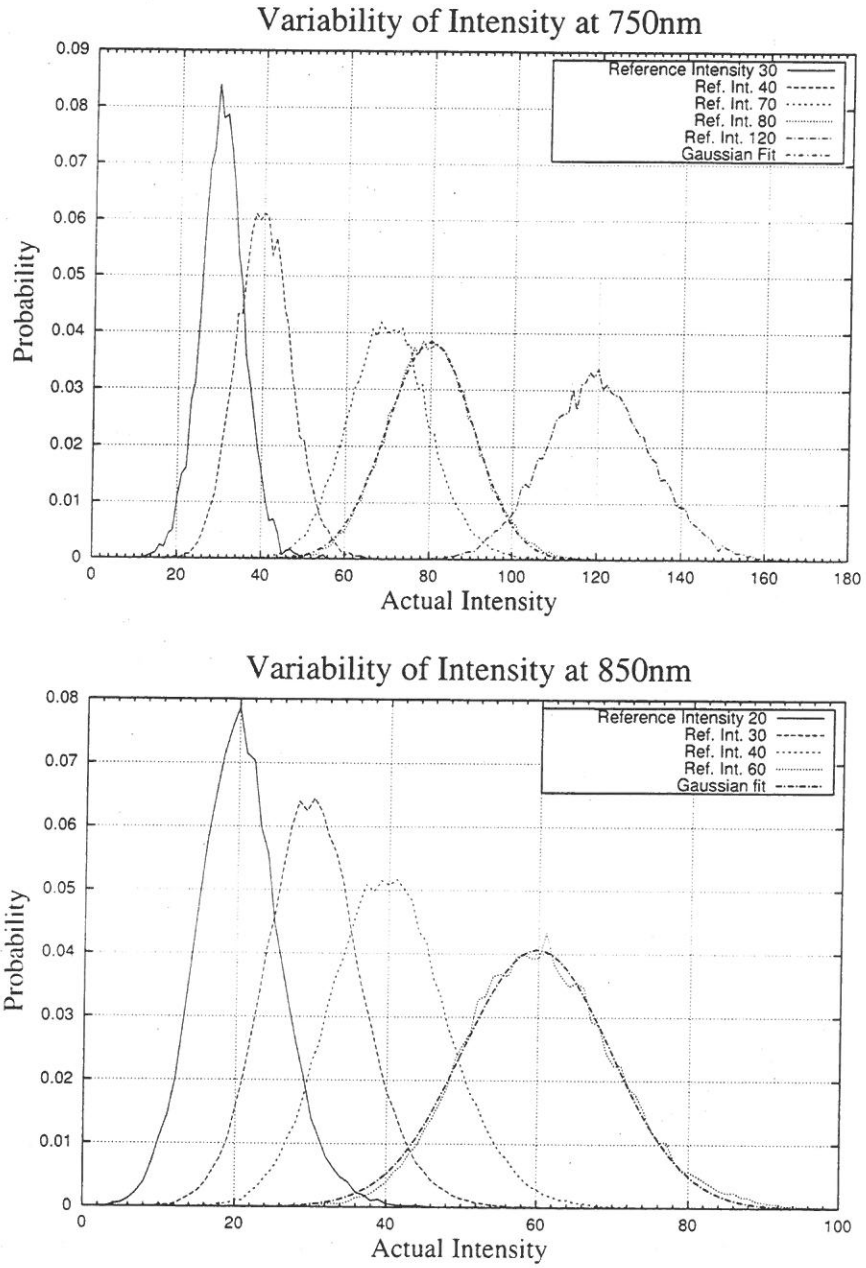

Figure 6: This figure shows the variability of the measured intensity in the present images. Each curve presents the probability density of the actual measured intensity with respect to a certain imposed reference intensity. Also shown is an exemplary Gaussian model fit to a single distribution. *Top* Variability at a wavelength of 750nm, *bottom* a similar plot for the images taken at a wavelength of 850nm. Note the different scalings of the abscissa of both plots.

stochastics):

$$\lim_{\mu\to\infty} p_p(z;\mu) = p_G(z;\mu,\sqrt{\mu}) \tag{10}$$

Plotting of the two corresponding distribution functions for reasonable (i.e. not too large) μ exactly reproduces the above skew. The skewness of a Poisson distribution having the mean μ varies with $\mu^{-1/2}$.

It is well-known though, that fluorescence imaging in a low intensity regime (i.e. counting of few photons) is a genuine Poisson process (see [4]). Typically this fact is neglected in many applications, and Gaussian distributed white noise is assumed instead. Anyhow, fig. 6 shows that for the used microscope working in the prevailing parameter range the white noise assumption is not very accurate. White noise would show a rather constant deviation. Instead a Poissonian noise distribution is clearly dominant. Obviously, for relatively high actual pixel intensities the noise is stronger than for low intensities and therefore the uncertainty of the real intensity is notably larger. This might seem to be contra-intuitive at first glance.

The "true" or reference pixel intensity g is proportional to the mean number μ of *detected* i.e. counted photons

$$g = \eta \cdot \mu\,, \tag{11}$$

where the factor η can be tuned by the microscope detector gain. Equation (10) predicts that the uncertainty $SD[g] = StD[p(g)]$ of a given intensity g (i.e. the SNR) is proportional to the square root of the number of counted photons:

$$SD[g] \propto \sqrt{\mu} = \frac{1}{\sqrt{\eta}} \cdot \sqrt{g} \tag{12}$$

This clearly relates to eq. (7), with the parameter a relating to the detector offset, and the parameter b gives a pre-amplification. So, the actual SNR increases with intensity. Furthermore fig. 6 shows clearly that the resulting *gray-level resolution*[7] is very low: The intensity dispersion curves for two reference intensities differing by a nominal pixel value of well 10 show a large overlap. Hence, a reliable retrospective estimation of the true

[7]Where the *spatial resolution* gives the minimum distance of two neighboring structures to be optically separable in an image, the gray-level resolution gives the minimum difference in discrete gray-levels two different pixels in an image must have, so that the respective intensities in the original scenery differ significantly.

intensity at a location $\mathbf{x}$ within measured data is a non-trivial task. There are two typical solutions to this problem:

(1) Application of de-noising techniques to the image data with the intention to increase the SNR. Techniques tailored to Poisson noise are preferable.

(2a) Reduction of the intensity quantization granularity i.e. the number of gray-levels present in the acquired images. This can be done by integer division of the measured discrete gray-levels by a reasonable divisor β, with the result that successive gray-levels in the resulting image are more separated with respect to counted photons (see [4]).

(2b) Another approach to reduce the number of quantization levels is described in [9]. A square root-based transformation on the pixel intensities is able to stabilize the noise, so that the data seems to come from a Gaussian instead of a Poisson random process.

Solution (1) has the potential advantage of not decreasing the range of gray-levels in the images, i.e. the intensity dynamics. Reduced intensity dynamics might obscure important image details. However, there is no global solution for the reduction of Poisson noise in arbitrary image data available yet. For solution (2a), in terms of counted photons, the single pixel intensity levels should be separated by about $\beta = \sqrt{\mu_{max}}$, where μ_{max} is the number of photons counted for the highest detected intensity in the image (see [4]). Pragmatically one can try to directly obtain this value from original images by careful examination of very high intense image regions, which are known to be homogenous. Doing so for the present images would leave only about 10 distinct pixel gray-levels in both image sets, which is a rather small number. However, knowledge of the parameter β can be useful also for adjustment of potential de-noising methods.

For low pixel intensities ($g < 30$) in fig. 5 the noise is much stronger than the Poisson photon counting model predicts. This is due to other noise sources in the imaging device, such as dark current and amplifier noise (see [4]). In the very low intensity regime these effects dominate the Poisson noise. The upper ends of both StD-curves are rather noisy due to the few accounted samples for the respective estimation.

In the case of high photon flux imaging (i.e. large μ) as e.g. in photography, the parameter η in eq. (11) becomes very small. The linear pixel intensity dependence on

η dominates the square root proportional relation of the noise intensity, and the Poisson noise is neglectable then.

4.2.3 Variability Comparison at different Excitation Wavelengths

Fig. 6 shows how a particular reference intensity g disperses at different excitation wavelengths λ_{ex}. Differences become more clear from fig. 7. For two different reference intensities and for both images series, the variation of actual intensity is shown. Additionally, fits of Gaussian normal distributions are given. The respective parameters can be found in table 3.

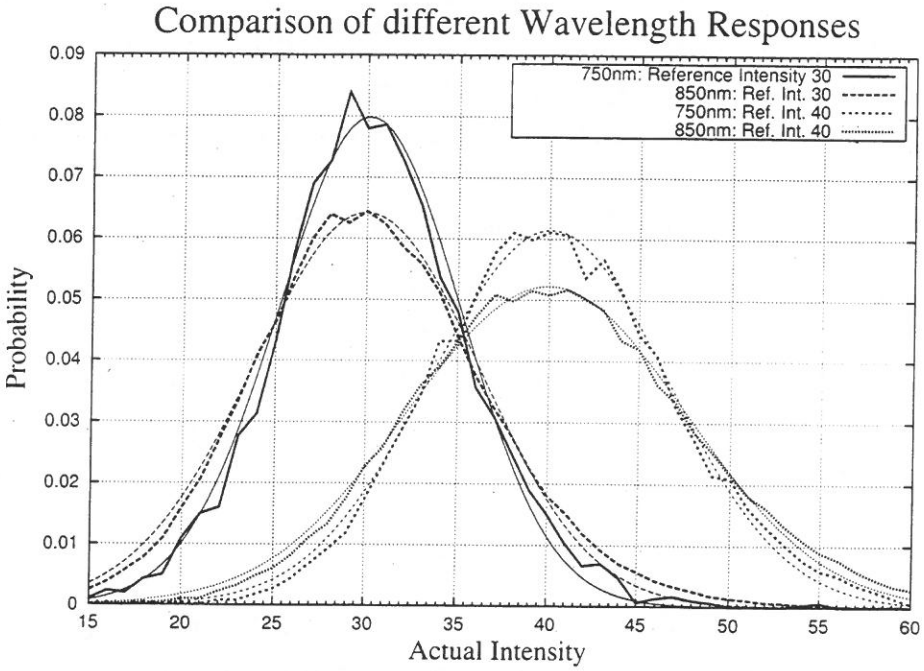

Figure 7: This plot compares the intensity distributions of two concrete reference intensities for both excitation wavelengths. Corresponding Gaussian fits are shown as thin lines.

Again, the typical Poisson to Gaussian deviations are clearly visible in the plots as are the differences for both excitation wavelengths. The two 750nm curves are noisier because less samples are available for the according reference intensity estimations (compare the histograms in fig. 5).

The factor of approx. 1.2 between the variabilities for both wavelengths visible in

Ref. Int.	30	40	50	60
750nm	4.99	6.49	7.73	8.68
850nm	6.21	7.64	8.82	9.81
·/·	1.24	1.18	1.14	1.13

Table 3: Gaussian Fit Standard Deviations according to fig. 7. The last line gives the quotient for the according both standard deviations.

table 3 stems from, according to eq. (12), an almost 40 percent increase[8] of resulting fluorescence photons in the 850*nm* case. But at the same time the detector sensibility for the resulting emission wavelength decreases by a net factor of about 2.3 with respect to the much brighter 750nm illuminated flatfield. The median values of all pixel intensity values for both reference images, which are taken as mean global intensities here, are 85 and 36, respectively. The median value is less sensitive to noise than the mean value.

4.2.4 Direct Poisson Modeling of Noise Distributions

Of course it is possible to directly use the Poisson function for modeling the intensity distribution of a given reference intensity g in the examined images instead of a Gaussian normal distribution. In this case the detector pre-amplification mentioned above has to be taken into account. The Poisson distribution function then gains a second degree of freedom, the shift ζ and reads:

$$p(z) = p_p(z+\zeta;\sigma^2)\,, \tag{13}$$

with z being the measured random intensity, $\zeta = \sigma^2 - g$, and σ and g are again the standard deviation and reference intensity of the respective intensity distribution. Both parameters can be estimated from the sampled distributions.[9] A comparison plot of the differences of Gaussian and Poisson modelled distributions is given in fig. 8. The Poisson model does a slightly better job in describing the data, but this advantage vanishes for increasing

[8] This effect depends on the actually imaged fluorochrome.

[9] The mean and standard deviation can be either estimated from the samples directly using eq. (1) or estimated by a fit of the assumed distribution function to the histogram of the samples. The fitting method generates slightly more accurate results in terms of the summed squares of residual values (*SSR*). E.g., for $g = 40$ and $\lambda_{ex} = 750nm$, $SSR = 2.2 \cdot 10^{-4}$ for the standard estimation, and $SSR = 1.2 \cdot 10^{-4}$ for the fit.

intensities. Anyhow, we still prefer using the Gaussian model in this work for its ease of use with respect to further statistical analysis of the noise distributions.

Note that the discrete eq. (9) is not very suitable for doing a nonlinear least squares fit. Instead a continuous analogon p of the Poisson probability function p_p can be formulated:

$$p(z;\mu) = \exp\left(-\mu + z\log\mu - \log\Gamma(z+1)\right) , \tag{14}$$

where $\log\Gamma(\cdot)$ is the natural logarithm of the Gamma-function, which substitutes the factorial in the original equation. The factorial is the one term that effectively discretizes eq. (9). The logarithm of the Γ-function is computeable more efficiently than the Γ-function itself (see [6]).

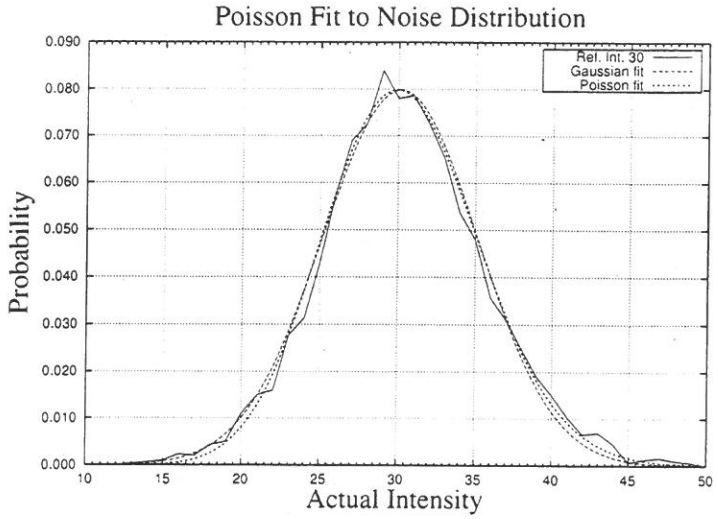

Figure 8: Comparison between Poisson and Gaussian distribution functions modeling an intensity distribution for a reference intensity of $g = 30$.

5 Conclusions and Prospectives

In this work it was shown, that examination of a set of laser scanning fluorescence flatfield images taken under absolutely the same imaging conditions can be fruitful in order to characterize the actual imaging process and its noise properties. Precise knowledge of a measurement process is fundamental for successful automatic data analysis. Detailed

quantitative information on the actual intensity variability due to noise of a laser scanning microscope was presented in this work.

Although using instrument parameters being similar as in typical specimen exploratory situations, the overall imaging conditions were quite artificial for the images examined in this work. However, it has become clear that the fluorescence intensity mapping is actually a notable Poisson process in this case. The often preferred Gaussian white noise approximation does not hold very well for the used microscope. In cases where the detector can not be optimized in its efficiency or where the output signal yield can not be increased by any kind of contrast enhancement, the Poissonian nature of the noise must be taken into account when automatic data processing techniques as e.g. de-noising and segmentation shall be applied to observed data. For example, the use of locally adaptive filters might be necessary for processing the MPLSM images. This depends on the specific object domain.

Additionally, the small distinctness of pixel intensity levels when imaging within the low intensity Poisson regime is a problem with respect to image contrast. The number of statistically differentiable gray-levels is reciprocal to the noise amount of the actual maximum intensity. A method to automatically detect and adjust the number of admissible distinct intensity levels in acquired images of a given domain is left here as an open problem. The intensity dispersions discussed in this report are very similar to the *intensity spread function*, as proposed by Pawley [3].

Furthermore, the noise dependency of actual illumination wavelength and detector sensitivity at the resulting emission wavelength was shown. Since the illumination laser of the used microscope is accurately tuneable, an optimized parameter adjustment in terms of specimen molecules and illumination wavelength may be utilized to prospectively enhance image contrast.

Further investigations might now involve phantom images showing very simple structures such as step edges in order to examine the intensity variation and shading influence on contrast, too. Imaging thin calibrating grids or fluorescence beads showing strong intensity contrast and again utilizing the shading effect and the characteristic noise would give information about how the resolution depends on local signal intensity. Sharp edges being perpendicular to the fast scanning direction and showing very high contrast can help in examining the dynamic properties of the PMT detector, as e.g. potential hystere-

sis effects in the output signal. True volume imaging and the effect of *depth of focus* (DOF) on the noise should be examined additionally. The DOF, which can be tuned by the microscope aperture, relates to the local volume that is illuminated to form one voxel of the resulting data set. Also of interest might be a more thorough validation of intensity variability at differing combinations of excitation wavelengths, fluorochromes, and illumination intensity. A reproducibility verification of the above given results is desirable. At last, an extension of the described approach to other instrument classes as e.g. confocal microscopy might be fruitful.

6 Acknowledgments

This work has been carried out by a grant from the Beiersdorf AG, Hamburg in the project: "Automatic analysis of LSM images", which started with the beginning of the year 2003. I thank Stefan Puschmann and Frank Fischer at Beiersdorf AG for their support in acquiring all the examined flatfield images and for technical discussion on multiphoton microscopy. Also I wish to thank my academic advisor H. Siegfried Stiehl at KOGS and Roger Wepf at Beiersdorf for many fruitful discussions and inspirations in the field of signal analysis.

References

[1] Alberto Diaspro, editor. *Confocal and Two-Photon Microscopy: Foundations, Applications, and Advances*. Wiley-Liss, Inc., New York, 2002.

[2] J. Pawley. *Handbook of Biological Confocal Microscopy*. Plenum Press NY, 1995.

[3] J. Pawley. The intensity spread function (isf): A new metric of photodetector performance. In A. Diaspro, F. Brakenhoff, and C. Usai, editors, *Focus on Microscopy*, page 107. University of Genova, 2003.

[4] J.B. Pawley. *Three-Dimensional Confocal Microscopy*, volume Investigation of Biological Specimens, chapter 3 - Sources of Noise in Three-Dimensional Microscopical Data Sets. Academic Press, Inc., 1994.

[5] D. Peña and F.J. Prieto. Multivariate outlier detection and robust covariance matrix estimation. *Technometrics*, 43(3), August 2001.

[6] William H. Press, Saul A. Teukolsky, William T. Vetterling, and Brian P. Flannery. *Numerical Recipes in C++*. Cambridge University Press, 2002.

[7] C.D. Rahn. Laser Scanning Microscopy Flatfield Images Part II: Characterization of Shading Effects. Technical report, University of Hamburg, Department of Informatics, Cognitive Systems Group, 2004. In preparation.

[8] M. Sonka, V. Hlavac, and R. Boyle. *Image Processing, Analysis and Machine Vision*. Chapman & Hall Computing, London, 1993.

[9] J.L. Starck and F. Murtagh. Astronomical image and signal processing - looking at noise, information, and scale. *IEEE Signal Processing Magazine*, March 2001.